



First-principles calculations of structural, magneto-electronic, mechanical, optical and thermoelectric properties of novel quaternary Heusler alloys type ZrCoYAs (Y= Fe and Mn)



O. Baraka ^{a,b,*}, S. Malki ^c, L. El farh ^c, A. Yakoubi ^a, D. Sébilleau ^d

^a Laboratoire D'étude des Matériaux & Instrumentations Optiques, Djillali Liabès University, Sidi Bel-Abbès, 22000, Algeria

^b Department of Process Engineering, Faculty of Technology, Hassiba Benbouali University of Chlef, 02000, Algeria

^c Physics Department, Faculty of Sciences, Mohammed 1st University, Oujda, Morocco

^d Univ. Rennes, CNRS, IPR (Institut de Physique de Rennes) - UMR 6251, F-35000, Rennes, France

ARTICLE INFO

Communicated by: Francois Peeters

Keywords:

DFT
Equiatomic quaternary Heusler
Half-metal
Magnetic properties
Thermoelectric properties

ABSTRACT

To determine the structural, mechanical, electronic, magnetic, optical, and thermoelectric properties of novel quaternary Heusler alloys type ZrCoYAs (Y= Fe and Mn), we used DFT with WIEN2k. Our results showed that the ferromagnetic Y-type-III phase is more stable due to the higher negative values of their formation energy. We calculated and discussed the elastic constants C_{ij} , which are used to calculate the mechanical properties. The Spin-polarized band structure and DOS calculations using the GGA-PBE and GGA + U approach display a metallic character. However, using the mBJ-GGA-PBE and mBJ-GGA + U approach show a half-metallic character, a semiconductor for the spin-down channel with a direct band gap of 0.61 eV with mBJ-GGA-PBE and 0.74 eV with mBJ-GGA + U for ZrCoMnAs and a direct band gap of 0.43 eV with mBJ-GGA-PBE and indirect band gap with 0.39 eV with mBJ-GGA + U for ZrCoFeAs, in contrast, the spin-up channel is metallic, with 100 % spin polarization and an integer magnetic moment of 1.00 μ B for ZrCoMnAs and 2.00 μ B for ZrCoFeAs, obeying the Slater-Pauling rule. The estimated Curie temperatures of ZrCoMnAs and ZrCoFeAs are 204 K using the new model, 421 K using MFA, and 385 K using the new model, 1627 K using MFA, respectively. As exchange-correlation potential, MBJ and MBJ + U provide a better description of the electronic and magnetic properties of ZrCoMnAs and ZrCoFeAs compounds. Important optical properties such as dielectric function, absorption coefficient, refractive index, optical conductivity, reflectivity, and electron energy loss function are calculated in the infrared, visible, and ultraviolet range. The static dielectric function suggests that ZrCoMnAs possesses greater polarizability. Both alloys exhibit similar behavior in the far ultraviolet region range and reach a maximum absorption in the ultraviolet range. The half-metallic character of both alloys is revealed from the reflectivity at zero frequency. The calculation of the thermoelectric properties shows positive Seebeck coefficients, indicating that these Heuslers are p-type. Furthermore, the highest power factor is observed at a temperature of 1400 K. The maximum value of ZT is ~1.1 at 1400 K for ZrCoFeAs and ZrCoMnAs. These studies show that these alloys may have potential applications in the thermoelectric applications.

1. Introduction

Heusler alloys are a unique class of materials with over 3000 alloys that can contain almost all of the periodic table's elements [1]. These materials display a wide range of property types, including half-metals compounds, spin-gapless semiconductors, high-temperature ferrimagnets and ferromagnets, antiferromagnets, materials with multiple ferroic properties, alloys with memory-shape properties, materials exhibiting

Weyl or Dirac semimetallic behavior, and adjustable topological insulators [2]. These characteristics would allow them to be used in fields such as spintronics, energy and magneto-caloric technologies [1,3,4], optoelectronic [5], and thermoelectricity [6]. The discovery of these unique alloys was made by Fritz Heusler in 1903 while examining the ferromagnetism of an alloy with the composition of Cu_2MnAl [7].

Heusler alloys are ternary intermetallic alloys with face-centered cubic crystal structure. These alloys are typically divided into two

* Corresponding author. Laboratoire d'étude des Matériaux & Instrumentations Optiques, Djillali Liabès University, Sidi Bel-Abbès, 22000, Algeria.
E-mail address: b.oussama@univ-chlef.dz (O. Baraka).

groups: those having 1:1:1 stoichiometry (XYZ Half-Heusler) and those having 2:1:1 stoichiometry (X_2YZ Full Heusler), where X and Y are transition metals, and Z is an element of III-V groups. The cubic L₂1 structure (space group Fm-3m, #225) of full Heusler alloys has four interpenetrating fcc sublattices. A quaternary Heusler structure with a distinct structural symmetry (space group F-43m, #216) is created when different atoms (XX'YZ) occupy each of these sublattices. LiMgPdSn type or Y-type is the name given to the resulting structure [8–10]. The quaternary alloys are known as equiatomic quaternary Heusler alloys due to the 1:1:1:1 stoichiometry.

Due to the additional disorder scattering caused by the random distribution of Y and Y' in pseudo-ternary alloys like $X_2Y_{1-x}Y'_xZ$, the spin diffusion length of equiatomic quaternary Heusler alloys is shorter than that of pseudo-ternary alloys, which has certain advantages over them from an application standpoint [11,12]. Devices based on XX'YZ are anticipated to have low power dissipations because there is no such scattering in XX'YZ [12]. The Heusler quaternary equiatomic has been experimentally synthesized or anticipated by first-principles calculations to exhibit several half-metallic ferromagnetisms: CoFeMnZ (Z = Al, Ga; Si, Ge, As) [13,14], CoFeTiSi, CoFeTiAs, CoFeVSB [15], and CoFe-TiGe [16], FeMnScZ (Z = Al, Ga, In) [17], CoRhMnGe and CoRhMnSi [18], CoMnTiZ (Z = P, As, and Sb) [19], CoMnCrSb [20], CoRuFeGe and CoRuFeSn [21], CoRuTiZ (Z = Si, Ge, and Sn) [22], CoRhMnGe [23], CoFeCrZ (Z = P, As and Sb) [24], CoCuMnSb [25], CoZrIrSi [26], CoYCrZ (Z = Si and Ge) [27], CoRuVAl [28], LaCoTiIn [29], CoRuVZ (Z = Si, Ge) [30].

Extensive research and development efforts are driven by the unique properties and diverse applications of Heusler quaternary alloys. Researchers aim to understand these materials better and exploit them to achieve technological progress in various fields.

Amidst the extensive research on Heusler alloys, this work distinguishes itself by introducing a novel half-metallic ferromagnetic equiatomic quaternary Heusler alloys type ZrCoYAs (Y = Fe and Mn). This breakthrough, supported by meticulous calculations of the structural, electronic, magnetic, mechanical, and thermoelectric properties, unveils a new frontier in the field. By highlighting the potential of these new alloys in revolutionary applications like spintronics, this research not only provides critical insights but also sparks excitement about the future possibilities in the field.

2. Method of calculations

An all-electron full-potential augmented plane waves approach [31], implemented in the Wien2k code [32], was utilized for the calculations, which are thought to be state-of-the-art for DFT calculations [33,34]. It was decided to use the GGA-PBE (Perdew-Burke-Ernzerhof generalized gradient approximation) [35,36] with a cut-off value of $R_{\text{mt}}K_{\text{max}} = 9$ for the plane wave expansion, where R_{mt} is the smallest atomic sphere radius and K_{max} is the largest reciprocal lattice vector used in the plane wave expansion, and $G_{\text{max}} = 14$ where G_{max} is defined as the accuracy of the Fourier expansion of the charge density. We have implemented the Hubbard factor as the exchange-correlation functional using the GGA + U method to study the on-site correlation of the transition metals [37]. For Co, Mn, and Fe atoms, the selected Hubbard coefficient U_{eff} values are 1eV for Co and Mn for ZrCoMnAs alloy and 1.1 eV for Co and Fe for ZrCoFeAs alloy. The mBJ potential, a modification of Becke and Johnson's exchange-correlation potential was used in the electronic structure and magnetic computations to accurately anticipate the size and nature of band gaps [38,39]. We have selected the muffin-tin radii 2.4 bohr for Zr and 2.2 bohr for Fe, Mn and As. 1500 Monkhorst-Pack special k-points were utilized in the Brillouin zone, equivalent to an $11 \times 11 \times 11$ centered k-mesh. The cut-off energy, which designates the separation of valence and core states throughout the self-consistency cycles, was set to -6 Ry, while the total energy convergence and charge density convergence tolerances were set to 10^{-4} Ry and 10^{-4} e, respectively.

3. Results and discussion

3.1. Structural properties

The equiatomic quaternary Heusler alloys crystallize in a face-centered cubic LiMgPdSn (Y-type) structure with the space group space group F-43m (#216) [8–10]. Fig. 1 illustrates the atomic arrangements of this type of structure as Y-type-I, Y-type-II, and Y-type-III. According to Table 1, the elements have Wyckoff positions of 4a (0,0,0), 4c (1/4, 1/4, 1/4), 4b (1/2, 1/2, 1/2), and 4d (3/4, 3/4, 3/4). To find the most stable atomic arrangement, we calculated the total energy as a function of volume for each of the three possible atomic arrangements, accounting for the paramagnetic (NM), ferromagnetic (FM), and anti-ferromagnetic (AFM) phases (Fig. 2). The results indicate that the ferromagnetic Y-type-III phase has a lower energy than the others, therefore the ferromagnetic Y-type-III for ZrCoMnAs and ZrCoFeAs is more stable than the Y-type-I and Y-type-II structures.

Following the data adjustment using Murnaghan's equation [40], we found the equilibrium lattice constant a , the bulk modulus B and its pressure derivative B' in their three different arrangements using GGA-PBE approximation. The results are grouped in Table 2.

The thermodynamic stability of these alloys is estimated from the formation energy (E_{form}) using the following formula:

$$E_{\text{for}}^{\text{ZrCoYAs}} = \frac{E_{\text{total}}^{\text{ZrCoYAs}} - (E_{\text{solid}}^{\text{Co}} + E_{\text{solid}}^{\text{Zr}} + E_{\text{solid}}^{\text{Y}} + E_{\text{solid}}^{\text{As}})}{4} \quad (1)$$

where $E_{\text{total}}^{\text{CoZrYAs}}$ represents the equilibrium total energy of ZrCoMnAs and ZrCoFeAs alloys, and $E_{\text{solid}}^{\text{Zr}}$, $E_{\text{solid}}^{\text{Co}}$, $E_{\text{solid}}^{\text{Y}}$ (Y = Fe and Mn), and $E_{\text{solid}}^{\text{As}}$ correspond to the total energies per atom in their stable structures, and 4 denotes the number of atoms in the unit cell.

The values of the formation energies, all negative, are presented in Table 2. Such negative values of E_{form} imply that the ZrCoYAs (Y = Fe and Mn) phases are thermodynamically stable. Then, since Y-type-III structures have the lowest E_{form} , so they are more stable than other types.

3.2. Elastic properties

Elastic properties let us understand the material strength for its technical applications while also offering a good and dynamic suggestion of the system. These constants provide a practical and essential understanding of solid mechanical stability under various forces. We investigated the elastic properties of ZrCoMnAs and ZrCoFeAs alloys using the method created by Morteza Jamal [41], which is implemented into the Wien2k code as the IRelast package. Just three independent elastic constants (C_{11} , C_{12} , and C_{44}) are used for materials with cubic structures. The results for elastic constants of the ZrCoMnAs and ZrCoFeAs alloys are listed in Table 3.

This table shows that the elastic constants C_{ij} for all alloys under study are positive and satisfy the Born-Huang conditions ($C_{11}+2C_{12} > 0$, $C_{11}-C_{12} > 0$, and $C_{44} > 0$) [42], and hence are mechanically stable.

Table 4 lists mechanical parameters that can be computed using the relations (2–9) [43], including Bulk modulus (B), Young's modulus (E), Shear modulus (G), Poisson's ratio (ν), Pugh's ratio (B/G), the anisotropic index (A), and Cauchy pressure (Cp).

$$E = \frac{9GB}{G + 3B} \quad (2)$$

$$B = \frac{1}{3}(C_{11} + 2C_{12}) \quad (3)$$

$$G_V = \frac{1}{5}(C_{11} - C_{12} + 3C_{44}) \quad (4)$$

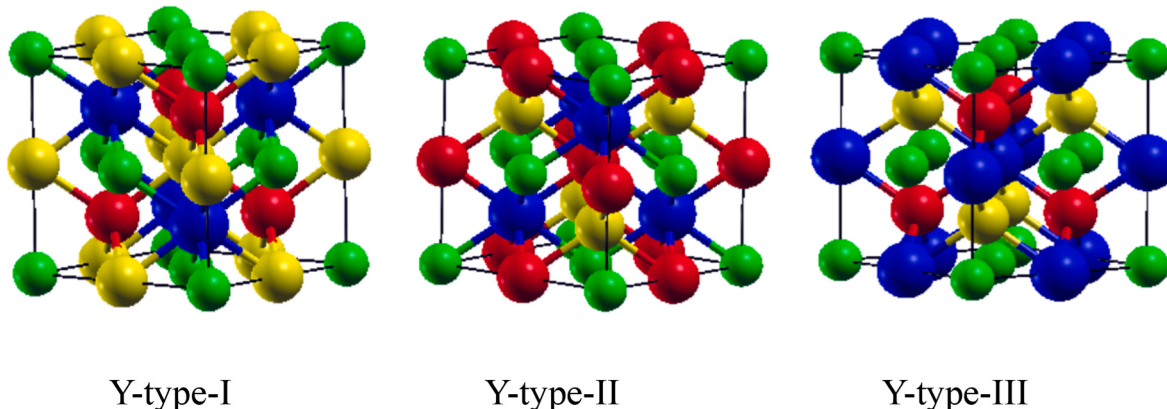


Fig. 1. The three different types of ZrCoYAs ($Y = \text{Fe}$ and Mn) quaternary Heusler alloys. (Yellow: Co, Blue: Zr, Red: Mn or Fe and Green: As).

Table 1

The Wyckoff positions of the atoms ZrCoYAs ($Y = \text{Fe}$ and Mn) quaternary Heusler alloys for three types of arrangements.

	Zr	Co	Fe	As
Y-type-I	$\frac{1}{4} \frac{1}{4} \frac{1}{4}$	$\frac{1}{2} \frac{1}{2} \frac{1}{2}$	$\frac{3}{4} \frac{3}{4} \frac{3}{4}$	0 0 0
Y-type-II	$\frac{1}{4} \frac{1}{4} \frac{1}{4}$	$\frac{3}{4} \frac{3}{4} \frac{3}{4}$	$\frac{1}{2} \frac{1}{2} \frac{1}{2}$	0 0 0
Y-type-III	$\frac{1}{2} \frac{1}{2} \frac{1}{2}$	$\frac{1}{4} \frac{1}{4} \frac{1}{4}$	$\frac{3}{4} \frac{3}{4} \frac{3}{4}$	0 0 0

$$\frac{5}{G_R} = \frac{4}{C_{11} - C_{12}} + \frac{3}{C_{44}} \quad (5)$$

$$G = \frac{1}{2}(G_V + G_R) \quad (6)$$

$$\nu = \frac{1}{2} \left[\frac{\left(B - \frac{2}{3}G \right)}{\left(B + \frac{1}{3}G \right)} \right] \quad (7)$$

$$A = \frac{2C_{44}}{C_{11} - C_{12}} \quad (8)$$

$$C_p = C_{12} - C_{44} \quad (9)$$

The value of Young's modulus, E , is 95.596 GPa for ZrCoMnAs and 116.083 GPa for ZrCoFeAs, which indicates that ZrCoFeAs is stiffer than ZrCoMnAs. The results of B obtained using the Muranghan equation of state (Table 2) coincide quite well with those determined from the

elastic constants, thus demonstrating the accuracy and precision of the latter.

From the results in Table 4, the Poisson's ratios ν of both materials are greater than 0.26, indicating that they are ductile and ionic [44]. The ductility of both materials is confirmed by the Pugh ratios (B/G) values, which are greater than 1.75. The positive values of the Cauchy pressure C_p also support this result.

The two alloys' anisotropic indices (A) differ from 1, meaning they have anisotropic elastic properties [43].

Another thermodynamic quantity is the melting temperature, estimated using the empiric formulation (10) [45,46].

$$T_{\text{melt}}(K) = (553 + 5.911 \times C_{11}) \pm 300 \quad (10)$$

The calculated melting temperatures are 1735.951 K for ZrCoMnAs and 1717.372 K for ZrCoFeAs, suggesting that both alloys can maintain their crystal structure over a wide temperature range.

3.3. Magnetic properties

The estimated local and total magnetic moments of the quaternary Heusler alloys ZrCoMnAs and ZrCoFeAs, as determined by the GGA-PBE, the mBJ-GGA-PBE, GGA + U and mBJ-GGA + U, are shown in Table 5. According to the Slater-Pauling rule, the total magnetic moment per formula unit M_{tot} is given by: $M_{\text{tot}} = Z_{\text{tot}} - 24$, where Z_{tot} is the total number of valence electrons [47]. An alloy cannot be a ferromagnetic half-metal unless M_{tot} has an integer value. Precisely, the total magnetic moments per formula unit M_{tot} calculated using the mBJ-GGA-PBE and mBJ-GGA + U method are found to be integer values, 1.00 μB for

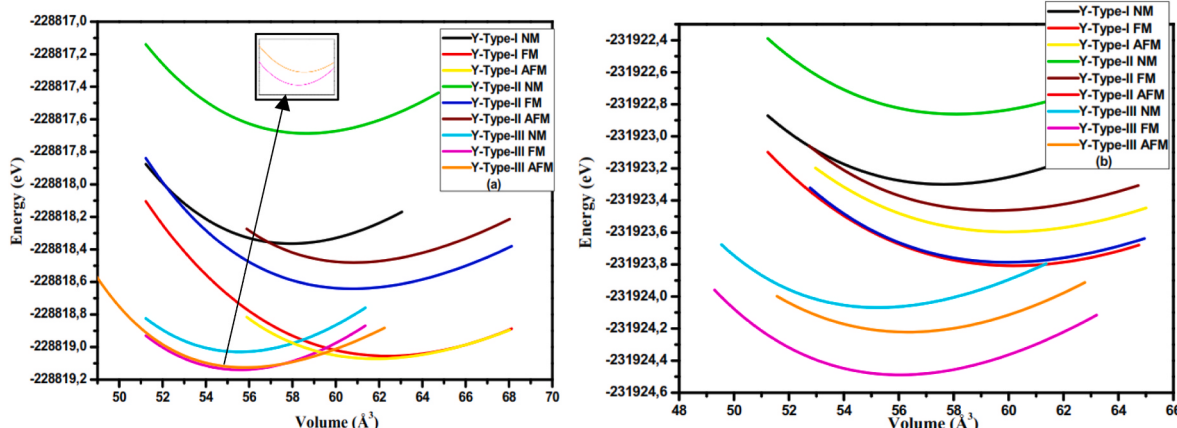


Fig. 2. The calculated total energy as a function of volume for all type in nonmagnetic (NM), ferromagnetic (FM), and antiferromagnetic (AFM) phases of (a) ZrCoMnAs and (b) ZrCoFeAs.

Table 2

The calculated structural parameters (a , B and B') and formation energy (E_{for}) of ZrCoMnAs and ZrCoFeAs quaternary Heusler alloys using GGA-PBE in Y-type-I, Y-type-II and Y-type-III structures in NM, FM, and AFM states.

		a (Å)	B (GPa)	B'	E_{for} (eV/atom)
ZrCoMnAs	Y-type- I NM	6.142	161.245	4.57	
	Y-type- I FM	6.296	115.867	3.27	-4.84
	Y-type- I AFM	6.277	112.592	5.96	
	Y-type- II NM	6.167	148.911	4.14	
	Y-type- II FM	6.240	119.369	5.52	-4.74
	Y-type- II AFM	6.243	132.134	6.54	
	Y-type- III NM	6.058	169.768	4.06	
	Y-type- III FM	6.058	170.775	4.23	-4.86
	Y-type- III AFM	6.066	141.762	6.74	
ZrCoFeAs	Y-type- I NM	6.132	157.763	3.99	
	Y-type- I FM	6.221	133.438	3.46	-5.47
	Y-type- I AFM	6.213	127.654	3.92	
	Y-type- II NM	6.148	148.045	4.39	
	Y-type- II FM	6.212	133.294	5.07	-5.47
	Y-type- II AFM	6.196	129.082	5.52	
	Y-type- III NM	6.045	163.991	6.00	
	Y-type- III FM	6.075	162.609	4.66	-5.64
	Y-type- III AFM	6.085	156.582	3.29	

Table 3

The calculated elastic constants for ZrCoMnAs and ZrCoFeAs quaternary Heusler alloys obtained using the GGA-PBE.

	C_{11} (GPa)	C_{12} (GPa)	C_{44} (GPa)
ZrCoMnAs	200.127	157.431	46.374
ZrCoFeAs	196.984	145.159	58.129

ZrCoMnAs (with $Z_{\text{tot}} = 25$) and 2.00 μB for ZrCoFeAs, (with $Z_{\text{tot}} = 26$), unlike the GGA and GGA + U method, which does not provide exact integer values. The As atom has a very modest magnetic moment compared to the other transition elements (Zr, Co, Mn and Fe), constituting the majority of the global magnetic moment.

In particular, for the electronic structure of materials, the modified Becke-Johnson (mBJ) potential provides a more accurate description of the exchange-correlation potential, which is crucial for accurately predicting the magnetic properties of materials, including their magnetic moments. Combined with GGA-PBE and GGA + U, it predicts magnetic moments consistent with the Slater-Pauling rule.

One way to estimate the Curie temperature is a new model proposed by Wurmehl et al., which is the linear relationship between the Curie temperature (T_C) and the total magnetic moments ($T_C = 23 + 181 M_{\text{tot}}$).

[28,48].

Additionally, the Mean-Field Approximation (MFA) was also used to estimate the Curie temperature using the given formula [28]:

$$T_C = \frac{\Delta E}{3K_B} \quad (11)$$

Where ΔE denotes the equilibrium energy difference between paramagnetic and ferromagnetic states, and K_B is the Boltzmann's constant.

The values found are 204 K using the new model, 421 K using MFA for ZrCoMnAs, 385 K using the new model and 1627 K using MFA for ZrCoFeAs. It is well recognized that MFA overestimates the Curie temperature. We do not have experimental results for comparison, but it is in the same range of T_C for Co-based quaternary Heusler alloys [30]. According to our findings, all of our alloys have Curie temperatures are higher than room temperature, meaning that spintronic device construction can use these materials.

3.4. Electronic properties

The spin-polarized band structure and spin-polarized density of states (DOS) calculations for ZrCoMnAs and ZrCoFeAs were carried out to explore the electronic properties.

The spin-polarized band structure profile was plotted along highly symmetric directions in Figs. 3–6 for spin-up and spin-down channels for ZrCoMnAs and ZrCoFeAs, using GGA-PBE, mBJ-GGA-PBE, GGA + U and mBJ-GGA + U respectively. Figs. 3 and 5 show that ZrCoMnAs and ZrCoFeAs have no band gap and thus act as a metal when treated with the GGA-PBE and GGA + U methods. However, when treated with mBJ-GGA-PBE and mBJ-GGA + U (Figs. 4 and 6), ZrCoMnAs and ZrCoFeAs act as a half-metal, giving metallic nature for spin-up channel and semiconducting characteristics with a direct band gap at symmetry point Γ (0.61 eV with mBJ-GGA-PBE and 0.74 eV with mBJ-GGA + U) for ZrCoMnAs for spin-down channel. For ZrCoFeAs, we see a direct band gap at symmetry point Γ with a value of 0.43 eV with mBJ-GGA-PBE and an indirect band gap in direction L to Γ with a value of 0.39 eV with mBJ-GGA + U for the spin-down channel.

Fig. 7 shows the total DOS of ZrCoMnAs and ZrCoFeAs obtained using GGA-PBE, mBJ-GGA-PBE, GGA + U and mBJ-GGA + U, whereas Figs. 8 and 9 shows the contribution from Zr, Co, (Mn or Fe), and As atoms using the mBJ-GGA-PBE and mBJ-GGA + U. The ratio of the contributions seen from the predicted DOS remains unchanged while moving from mBJ-GGA-PBE to mBJ-GGA + U. The energy levels between -8.0 and 4.0 eV were used to plot the DOS profile. The spin-up channel is represented by DOS on the positive y-axis side, while the

Table 4

The calculated Young's modulus (E), bulk modulus (B), shear modulus (G), Poisson's ratio (ν), the anisotropic index (A), Pugh's ratio (B/G), Cauchy pressure (Cp) and melting temperature (T_{mel}) for ZrCoMnAs and ZrCoFeAs quaternary Heusler alloys obtained using the GGA-PBE.

	E (GPa)	B (GPa)	G (GPa)	ν	A	B/G	Cp (GPa)	$T_{\text{mel}} \pm 300$ (K)
ZrCoMnAs	95.596	171.663	33.967	0.407	2.17	5.05	111.06	1735.951
ZrCoFeAs	116.083	162.434	42.032	0.380	2.24	3.86	87.03	1717.372

Table 5

Calculated total and local magnetic moments (in μ_B) for ZrCoMnAs and ZrCoFeAs quaternary Heusler alloys obtained using the GGA-PBE, mBJ-GGA-PBE, GGA + U, and the mBJ-GGA + U.

		$M^{\text{Zr}}(\mu_B)$	$M^{\text{Co}}(\mu_B)$	$M^{\text{Fe}}(\mu_B)$	$M^{\text{As}}(\mu_B)$	$M^{\text{int}}(\mu_B)$	$M^{\text{tot}}(\mu_B)$
ZrCoMnAs	GGA-PBE	-0.078	0.662	0.485	0.004	-0.077	0.997
	mBJ-GGA-PBE	-0.108	0.941	0.323	0.009	-0.167	1.000
	GGA + U	-0.071	0.722	0.418	0.007	-0.084	0.993
	mBJ-GGA + U	-0.066	1.013	0.189	0.013	-0.149	1.000
ZrCoFeAs	GGA-PBE	-0.143	1.069	1.140	0.039	-0.119	1.986
	mBJ-GGA-PBE	-0.259	1.256	1.271	0.046	-0.314	2.000
	GGA + U	-0.144	1.062	1.160	0.038	-0.151	1.964
	mBJ-GGA + U	-0.225	1.290	1.179	0.046	-0.289	2.000

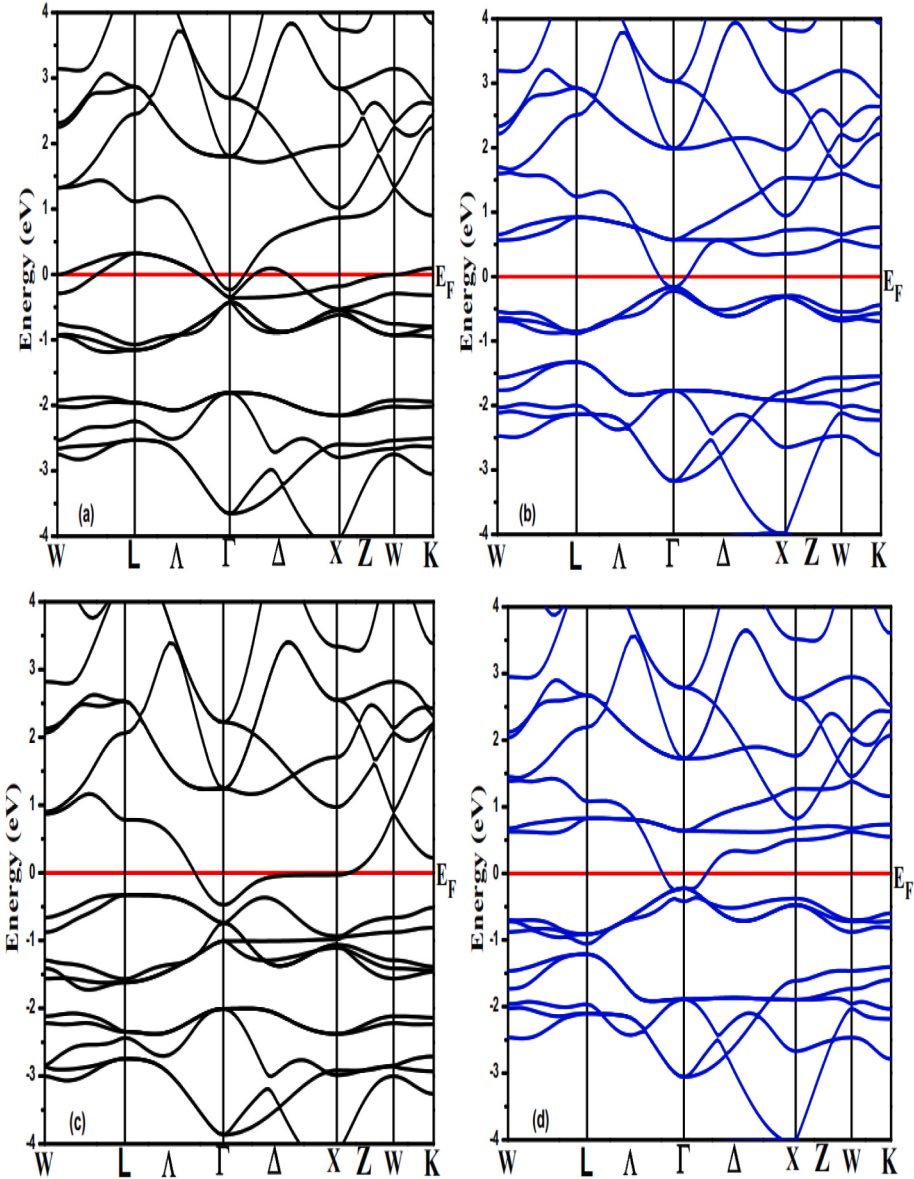


Fig. 3. Spin-polarized band structures of (a,b) ZrCoMnAs and (c,d) ZrCoFeAs, calculated at the equilibrium lattice constant using GGA-PBE for both majority (black) and minority (blue) spins. The horizontal red line indicates the Fermi level.

spin-down channel is shown on the negative y-axis. We find an energy gap in the minority spin states at the Fermi level. According to our earlier band structure discussion, these alloys exhibit a ferromagnetic half-metallic character.

The partial DOS indicates distinct electron distribution in the energy ranges: $[-7, -4]$ eV is dominated mainly by the p-As states, while the remaining region between -4 and 4 eV exhibits a strong hybridization of the 3d-Zr, 3d-Co, and 3d-Mn states. The hybridization of the d states of the Zr, Co, Fe and Mn atoms causes the gap and half-metal character in ZrCoMnAs and ZrCoFeAs.

The spin polarization can be calculated using the total density of states at the Fermi energy level using the following relation:

$$P = \frac{S_{\uparrow}(E_F) - S_{\downarrow}(E_F)}{S_{\uparrow}(E_F) + S_{\downarrow}(E_F)} \cdot 100 \quad (12)$$

Where $S_{\uparrow}(E_F)$ and $S_{\downarrow}(E_F)$ stand for the total density of states at the Fermi energy level of the majority and minority spin channels, respectively. ZrCoMnAs and ZrCoFeAs exhibit 100 % spin polarization due to their half-metallic nature (zero DOS in spin-down channel Fig. 7).

3.5. Optical properties

The optical properties of cubic ZrCoFeAs and ZrCoMnAs compounds are examined in the energy domain 0 – 14 eV, using the mBJ-GGA + U approximation. We have inspected refractive index $n(\omega)$, extinction coefficient $k(\omega)$, absorption coefficient $\alpha(\omega)$, optical conductivity $\sigma(\omega)$, reflectivity $R(\omega)$ and electron energy loss functional $L(\omega)$. All these parameters are deduced from the following complex frequency depending dielectric function:

$$\epsilon(\omega) = \epsilon_1(\omega) + i\epsilon_2(\omega) \quad (13)$$

The real and imaginary part $\epsilon_1(\omega)$ and $\epsilon_2(\omega)$ are calculated using the Kramers-Kronig relations [49,50]:

$$\epsilon_1(\omega) = \frac{2}{\pi} P \int_0^{\infty} \frac{\omega' \epsilon_2(\omega') d\omega'}{(\omega'^2 - \omega^2)} d\omega' \quad (14)$$

$$\epsilon_2(\omega) = -\frac{2\omega}{\pi} P \int_0^{\infty} \frac{\epsilon_1(\omega') d\omega'}{(\omega'^2 - \omega^2)} d\omega' \quad (15)$$

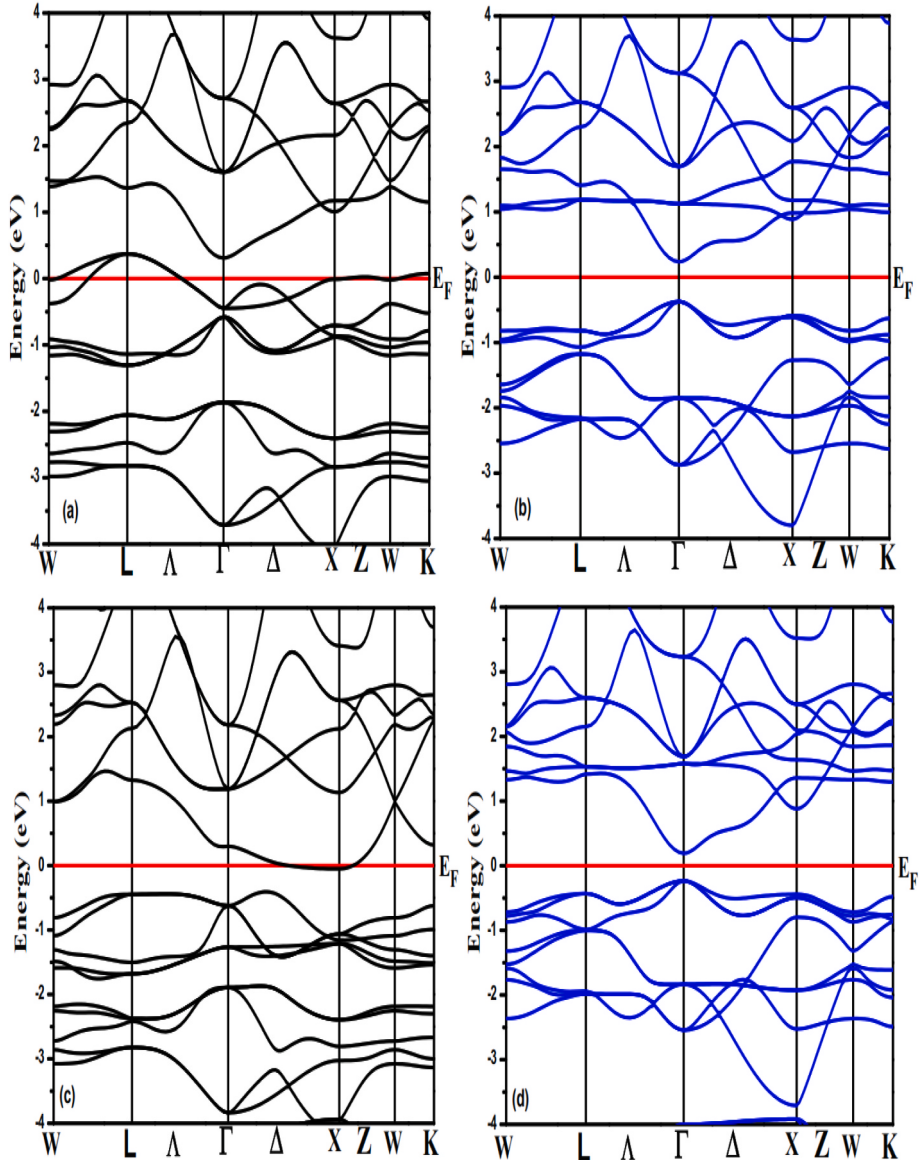


Fig. 4. Spin-polarized band structures of (a,b) ZrCoMnAs and (c,d) ZrCoFeAs, calculated at the equilibrium lattice constant using mBJ-GGA-PBE for both majority (black) and minority blue spins. The horizontal red line indicates the Fermi level.

Where P is designated as the Cauchy principal value of the integral.

Thus, all the optical properties depend completely on the components of dielectric function and frequency.

$$n(\omega) = \frac{1}{\sqrt{2}}((\varepsilon_1^2 + \varepsilon_2^2) + \varepsilon_1)^{\frac{1}{2}} \quad (16)$$

$$k(\omega) = \frac{1}{\sqrt{2}}((\varepsilon_1^2 + \varepsilon_2^2) - \varepsilon_1)^{\frac{1}{2}} \quad (17)$$

$$\sigma(\omega) = \frac{\omega}{4\pi}\varepsilon_2(\omega) \quad (18)$$

$$R(\omega) = \left| \frac{\sqrt{\varepsilon_1(\omega) + i\varepsilon_2(\omega)} - 1}{\sqrt{\varepsilon_1(\omega) + i\varepsilon_2(\omega)} + 1} \right| \quad (19)$$

$$L(\omega) = \frac{\varepsilon_2}{\varepsilon_1^2(\omega) + \varepsilon_2^2(\omega)} \quad (20)$$

$$\alpha(\omega) = \frac{\sqrt{2}\omega}{c} \left(\sqrt{\varepsilon_1^2(\omega) + \varepsilon_2^2(\omega)} - \varepsilon_1(\omega) \right)^{1/2} \quad (21)$$

Fig. 10 (a) represents the real parts $\varepsilon_1(\omega)$ of the dielectric function of the two compounds. The value of the static dielectric function of the ZrCoMnAs compound $\varepsilon_1(0) = 117$ is more larger than ZrCoFeAs $\varepsilon_1(0) = 33$, indicating greater polarizability for the former. After, $\varepsilon_1(\omega)$ of ZrCoFeAs and ZrCoMnAs shows three peaks at 0.5 eV, 1.8 and 2.7 eV for ZrCoFeAs and at 1.1 eV, 1.9 eV and 2.3 eV for the ZrCoMnAs using mBJ + U. These peaks are located in the infrared and visible regions (0.4–2.5 eV). Beyond 3 eV, $\varepsilon_1(\omega)$ is negative then tends to 0. The stable values of $\varepsilon_1(\omega)$ of both compounds indicate that the incident electromagnetic radiation does not interact significantly with the material.

The $\varepsilon_2(\omega)$ curves of two compounds presented in **Fig. 10 (b)**. They describes the interband transitions from the filled band (valence band) to the unoccupied one above (conduction band), as well as the absorption of electromagnetic emission incident on the compound [51,52]. In the case of ZrCoMnAs, $\varepsilon_2(0) = 45.6$, and $\varepsilon_2(\omega)$ shows a first peak in the infrared domain at around 0.3. There are also 3 peaks in the visible at about 0.1, 1.3 and 2.6 eV. Other peaks are also observed in the

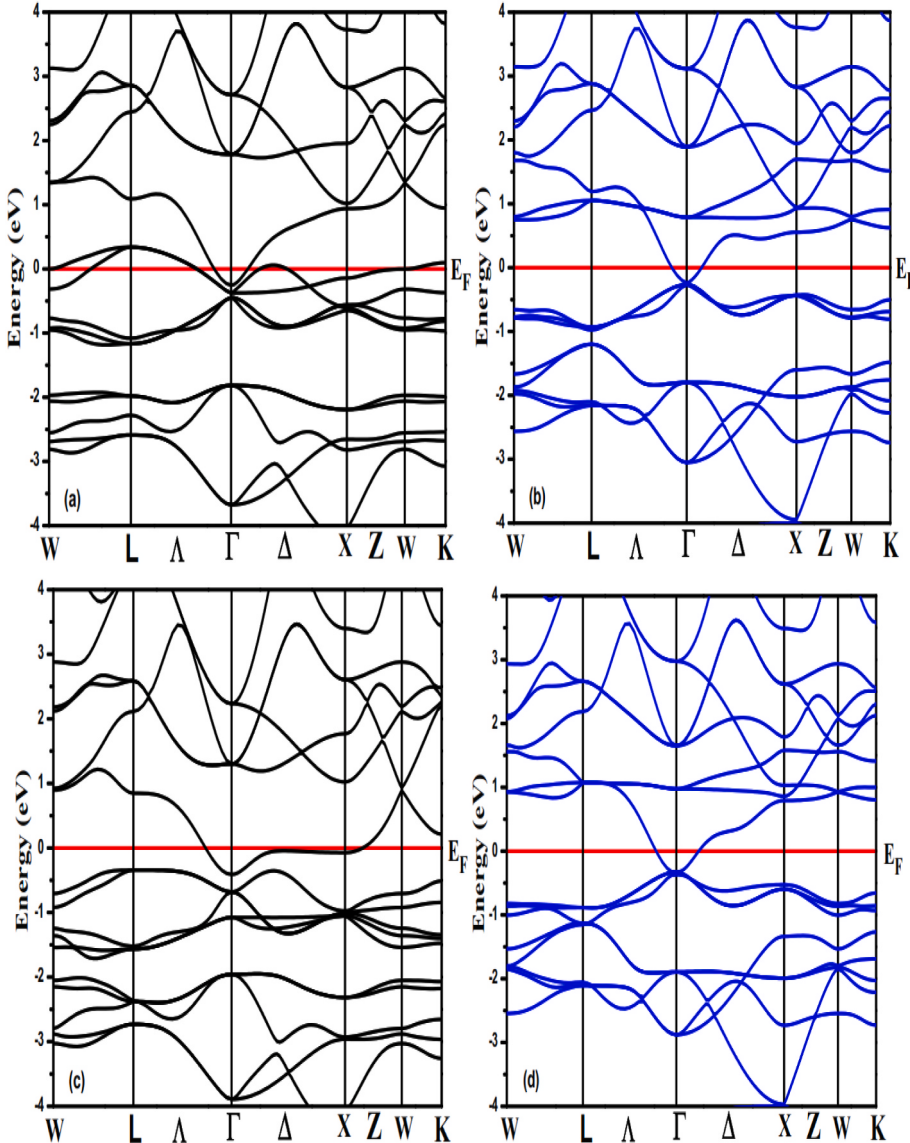


Fig. 5. Spin-polarized band structures of (a,b) ZrCoMnAs and (c,d) ZrCoFeAs, calculated at the equilibrium lattice constant using GGA + U for both majority (black) and minority blue) spins. The horizontal red line indicates the Fermi level.

ultraviolet. For ZrCoFeAs, $\epsilon_2(0) = 1.1$, and we note a first peak in infrared at about 0.6 eV. The $\epsilon_2(\omega)$ also shows 3 peaks in the visible at about 0.64, 2.2 and 2.9 eV and other peaks are present in the UV region (see Fig. 11).

Fig. 11 (a) illustrates the refractive index curves of ZrCoYAs (Y = Fe and Mn) using mBJ + U approximation, having a cubic structure. The study of this property is very important for photoelectric applications. The static refractive index $n(0)$ is about 5.8 for the ZrCoFeAs compound, and it is about 11 for ZrCoMnAs, almost 2 times greater. In the previous results, we verify the relation $n^2(0) \approx \epsilon_1(0)$.

The refractive index of each compound exhibits two predominant peaks, one in the infrared region and the second in the visible region, then $n(\omega)$ gradually decreases as the energy increase. The interband transition between the topmost valence band and the lowermost conduction band gives rise to these peaks. The nonlinear behavior of the refractive index is evident from the peaks observed in the infrared region.

Fig. 11 (b) displays the extinction coefficient $k(\omega)$, which signifies the extent to which incident photons can penetrate a material and also indicates any absorption losses. We notice that the curves of $k(\omega)$ align closely with those of the imaginary parts of the dielectric function of the

two compounds. The highest peak for ZrCoFeAs arises at 3.6 eV in the visible region, following that, the values of $k(\omega)$ exhibit a smooth decline in the near ultraviolet and middle ultraviolet ranges, and thereafter the peaks around 6.6 eV, the values of $k(\omega)$ consistently decrease in the far ultraviolet range. Around 7 eV, the refractive index and extinction coefficient become semiflat curves at high-energy ranges.

The absorption coefficient $\alpha(\omega)$ holds great significance when examining the characteristics of photon energy beams propagating through a material. From the curve illustrated in Fig. 12 (a), the absorption starts at 0.1 eV for ZrCoMnAs and 0.4 eV ZrCoFeAs, after overcoming the energy of the fundamental band gap energy.

In the infrared, visible and near ultraviolet regions, the absorption coefficient increases with increasing energy. In the mid-UV region, the absorption coefficient shows an almost stable behavior, with an average value of about 140 ($10^4/\text{cm}$). Finally, in the far ultraviolet region, the absorption is almost stable with an average value of about 180 ($10^4/\text{cm}$).

Fig. 12 (b) displays the energy loss function $L(\omega)$, also known as the electron energy loss spectrum (EELS). This spectrum illustrates the energy lost by electrons in a material due to their excitations when light passes through the material. The electron energy loss spectrums (EELS)

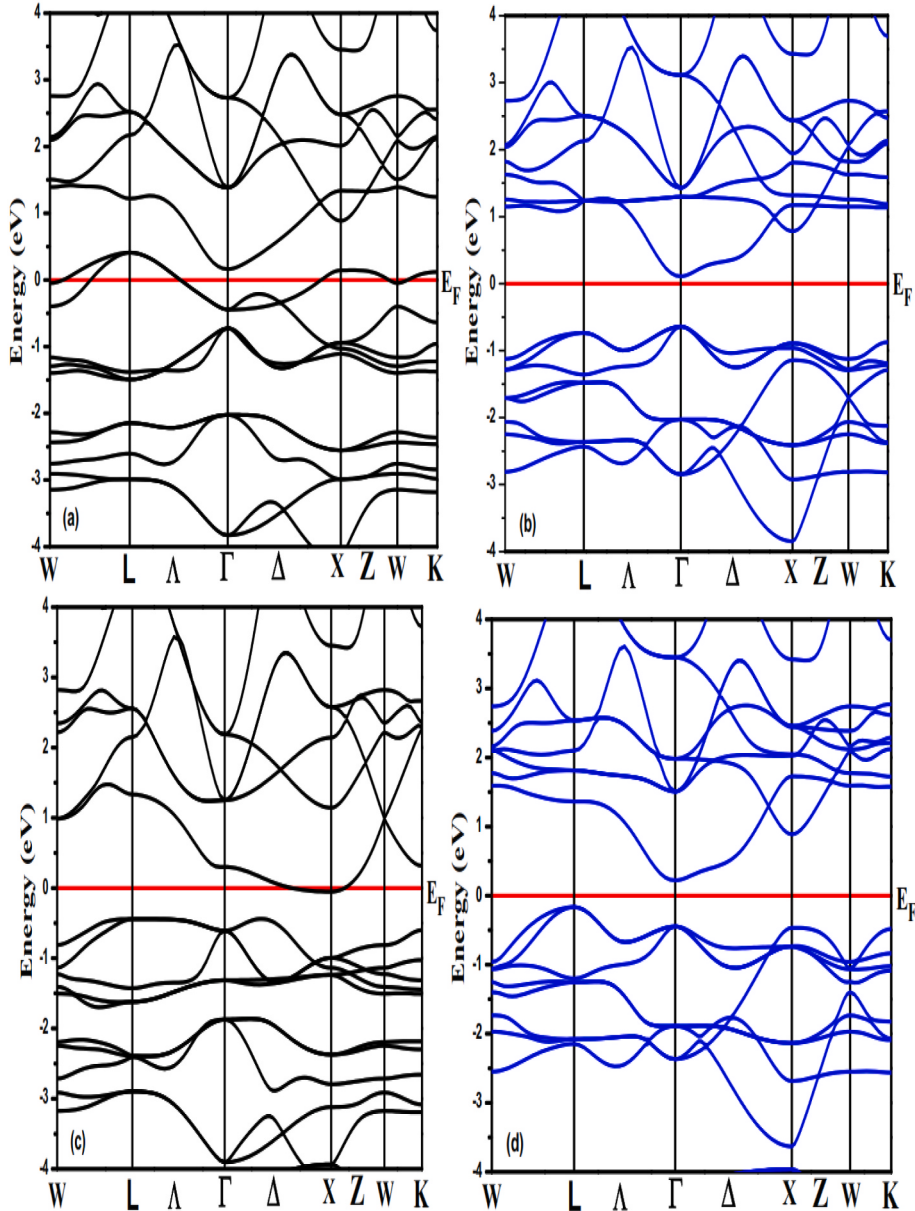


Fig. 6. Spin-polarized band structures of (a,b) ZrCoMnAs and (c,d) ZrCoFeAs, calculated at the equilibrium lattice constant using mBJ-GGA + U for both majority (black) and minority blue spins. The horizontal red line indicates the Fermi level.

show remarkably similar variations for both compounds. The main energy losses occur mainly in the UV region. In the infrared (IR) region, the energy losses are very low for both materials, with a peak at around 0.4 eV for ZrCoMnAs and 0.6 eV for ZrCoFeAs. The latter indicates the presence of a plasma resonance at this frequency, called plasma frequency [53,54].

The reflectivity spectra $R(\omega)$ of both compounds are depicted in Fig. 12 (c). It was observed that the reflectance at zero energy, $R(0)$, is 70 % for ZrCoMnAs and 50 % for ZrCoFeAs, which indicates that these compounds exhibit half-metallic characteristics. This is evident since it does not tend towards 100 % [55]. As the photon energy increases further, the reflectivity also increases and reaches multiple peaks, which are identical, displaying similar characteristics along the infrared, visible, and ultraviolet regions.

The maximum peaks observed in the UV region also exhibit nearly identical percentages of reflectance in both compounds. The low reflectivity and high absorption coefficient in the visible ultraviolet region make this compound a potential candidate for applications of solar

cells and optoelectronic devices [56].

The optical conductivity curves, depicted in Fig. 12 (d), provide insights into the conductance behavior of a compound under optical excitation induced by incident photon energy beams.

It is observed that the optical conductivity of both compounds reaches its maximum value in the visible region. This indicates that ZrCoMnAs and ZrCoFeAs exhibit higher conductivity in this range.

We can notice multiple peaks for both compounds in the infrared, visible, and UV regions that decrease for higher energies.

3.6. Thermoelectric properties

Subsequently, we used the mBJ-GGA + U method to examine the thermoelectric characteristics influenced by spin in both alloys. In this context, we investigated various properties, including the Seebeck coefficient (S), electronic thermal conductivity (κ_e), electrical conductivity per relaxation time (σ/τ), power factor (PF), and figure of merit (ZT) as a temperature dependent analysis up to 1400 K. For an alloy to be

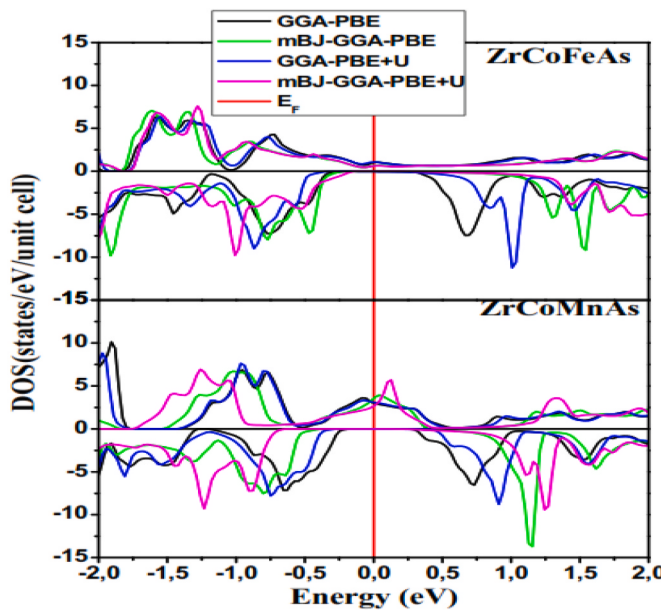


Fig. 7. Spin-polarized total DOS of ZrCoMnAs and ZrCoFeAs obtained using the GGA-PBE, GGA + U, mBJ-GGA-PBE, and mBJ-GGA + U.

considered a promising thermoelectric (TE) material, it should exhibit high values of both the Seebeck coefficient and electrical conductivity, while simultaneously demonstrating low thermal conductivity [57]. Ultimately, our focus was on evaluating the TE transport efficiency by examining the power factor and figure of merit, as they serve as key indicators in determining the overall performance.

Fig. 13 (a) illustrates the Seebeck coefficient (S) for both alloys, which represents their capability to generate a voltage or potential difference in response to temperature variations applied to materials. Positive values of the Seebeck coefficient (S) for both compounds indicate the prevalence of p-type carriers, where conduction is primarily

carried out by holes. The Seebeck coefficients generally increase with rising temperature up to approximately 1000 K. After reaching this point, the values stabilize and remain constant.

At room temperature, the values of the (S) for p-type carriers are 70 $\mu\text{V/K}$ for ZrCoMnAs, while for ZrCoFeAs is 50 $\mu\text{V/K}$.

The ability of an alloy to conduct heat is known as thermal conductivity, which arises from the vibrations of the alloy's lattice and electrons. It can be determined by adding the electronic and lattice thermal conductivities, denoted as $\kappa = \kappa_{\text{l}} + \kappa_{\text{e}}$. In our study, we have generated plots representing (κ_{e}) of the alloys, which is illustrated in **Fig. 13 (b)**.

The electronic thermal conductivity (κ_{e}) values exhibit a significant increase as the temperature rises. This increase is observed for both alloys. At 1400 K, the κ_{e} values reach their maximum values, ZrCoMnAs has $16 \times 10^{14} \text{ W/mK}$, and for ZrCoFeAs reaching $22 \times 10^{14} \text{ W/mK}$. This suggests that these alloys demonstrate enhanced heat conduction capabilities at higher temperatures. At room temperature, ZrCoMnAs has $5.6 \times 10^{14} \text{ W/mK}$, and for ZrCoFeAs reaching $7.8 \times 10^{14} \text{ W/mK}$ with higher κ_{e} values for ZrCoFeAs compared to the ZrCoMnAs alloy. After this temperature, it is significantly increases with a temperature rise for both alloys. The observed increase in electronic thermal conductivity with temperature can be attributed to the augmentation of electron vibration, leading to an increase in their energy levels. This character is greater in ZrCoFeAs than in ZrCoMnAs.

Fig. 13 (c) demonstrates the electrical conductivity per relaxation time ((σ/τ)), which accounts the electrical conductance of a material resulting from the movement of electrons between regions of high and low temperatures. Similar to κ_{e} , the values of (σ/τ) increase as the temperature rises. The inset figure shows the increase in electrical conductivity as a function of temperature for the ZrCoMnAs alloy. This trend is observed for both alloys. The maximum values at 1400 K are $1.3 \times 10^{20} \Omega/\text{ms}$ and $1 \times 10^{20} \Omega/\text{ms}$ for ZrCoFeAs and ZrCoMnAs, respectively. The increased number of charge carriers is typically responsible for the higher electrical conductivity observed in materials and room temperature values are $1.1 \times 10^{20} \Omega/\text{ms}$ and $1 \times 10^{20} \Omega/\text{ms}$. As a result of the relatively high conductivities, they could be used to fabricate high

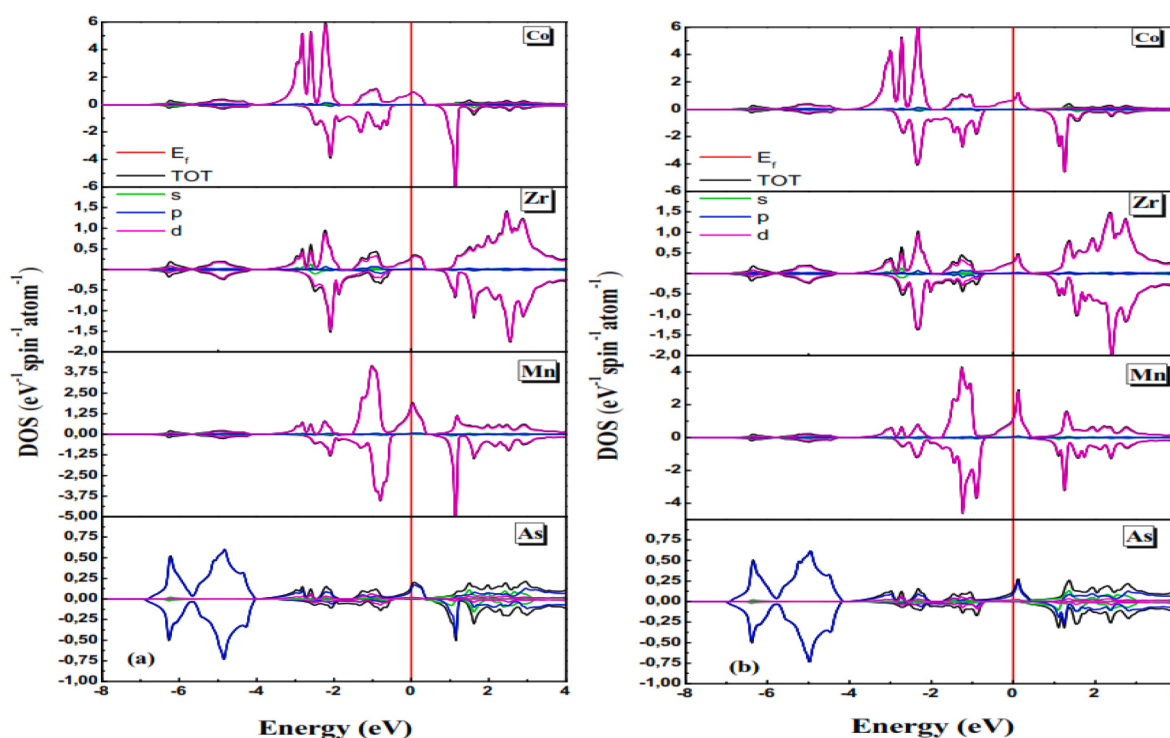


Fig. 8. Spin-polarized partial DOS of ZrCoMnAs obtained using the (a) mBJ-GGA-PBE and (b) mBJ-GGA + U.

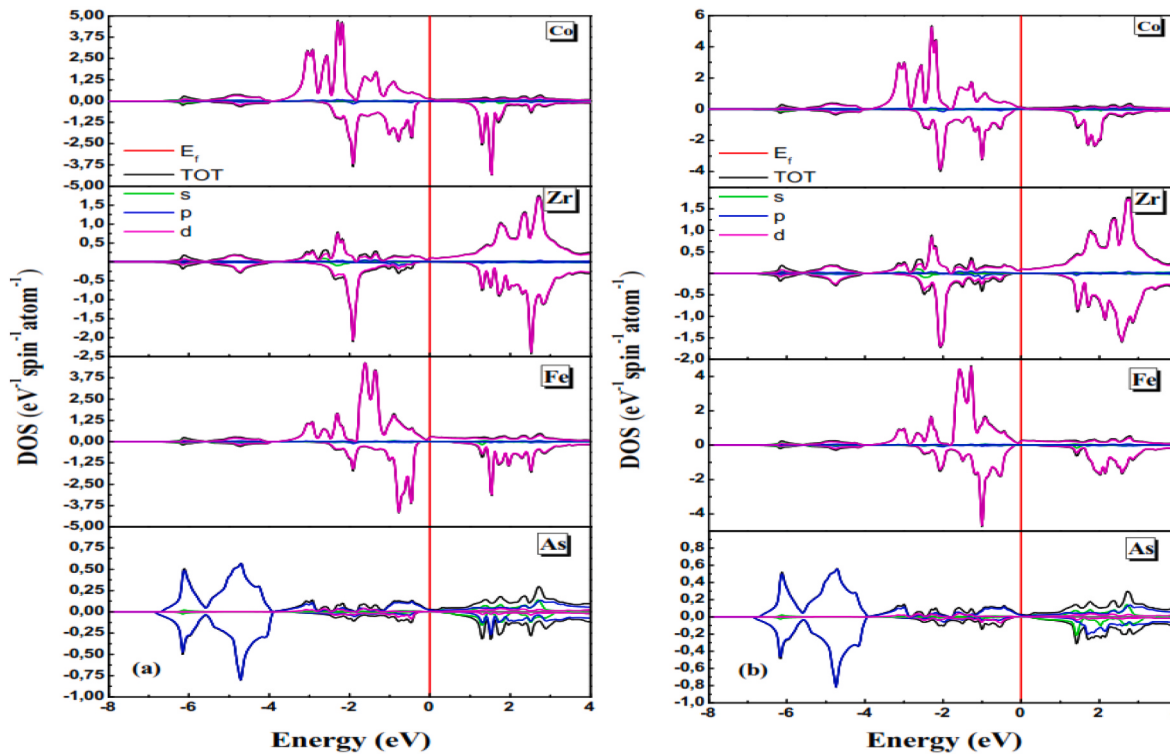


Fig. 9. Spin-polarized partial DOS of ZrCoFeAs obtained using the (a) mBJ-GGA-PBE and (b) mBJ-GGA + U.

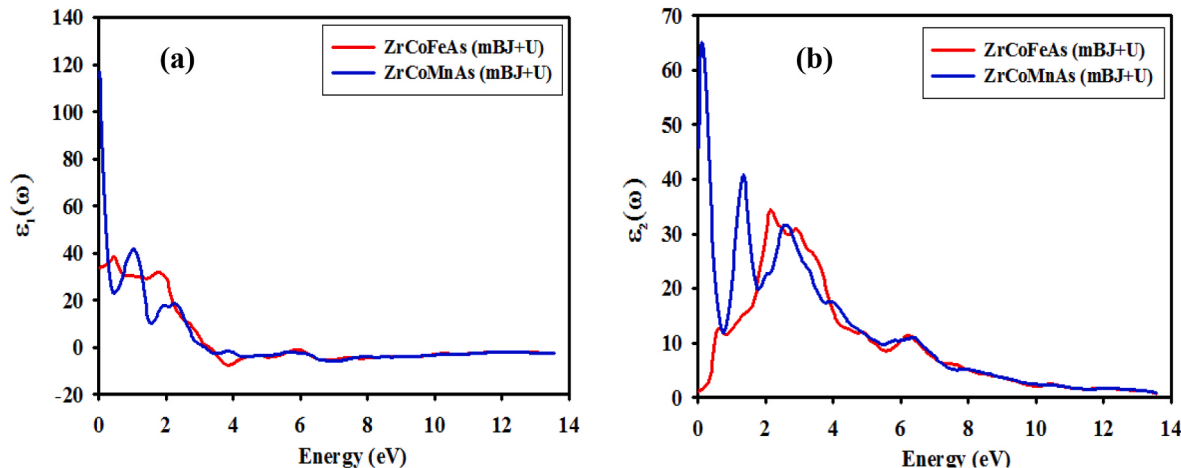


Fig. 10. (a) Real and (b) imaginary parts of the complex dielectric function.

temperature conductive components in the aerospace industry [58].

The magnetic susceptibility (χ) describes the magnetic properties of materials when subjected to an external magnetic field. Fig. 13 (d) illustrates the variation of magnetic susceptibility (χ) for ZrCoFeAs and ZrCoMnAs alloys. It is clear from the result that the magnetization of ZrCoMnAs compound increased linearly with temperature and has a maximum value of (χ) at 1400K because it has high exchange constants, which depend on the carrier concentration [59]. For ZrCoFeAs alloy, this properly does not follow Curie law, i.e., $\chi \propto 1/T$ [60], and other magnetic behaviors as well. This confirms that ZrCoFeAs is a nonmagnetic or diamagnetic. This characteristic is evident in multiple alloys [61–63].

Additionally, Fig. 14 (a) depicts the power factor (PF) of these alloys as a function of temperature. The power factor (PF) is expressed as $PF = S^2\sigma/\tau$, where S represents the Seebeck coefficient and σ/τ relates to the

electrical conductivity. This equation is a fundamental aspect of investigating the transport characteristics of a thermoelectric (TE) material. With increased temperature, the power factor values for both alloys exhibit a linear increase up to around 600K, after which the power factor of ZrCoFeAs surpasses that of ZrCoMnAs. Therefore, the significant linear increase in PF indicates the strong potential of both alloys for commercial thermoelectric applications [64]. The maximum PF value at 1400 K is $1.7 \times 10^{12} \text{ W/K}^2.\text{ms}$ and $1.3 \times 10^{12} \text{ W/K}^2.\text{ms}$ for ZrCoFeAs and ZrCoMnAs, respectively.

After considering all the thermoelectric (TE) properties, we have calculated the dimensionless figure of merit (ZT). ZT is widely regarded as the most crucial parameter for assessing the effectiveness of TE material. It serves as an indicator of the material's thermoelectric performance and provides valuable insights into its efficiency in converting heat into electricity. The dimensionless (ZT) can be directly associated

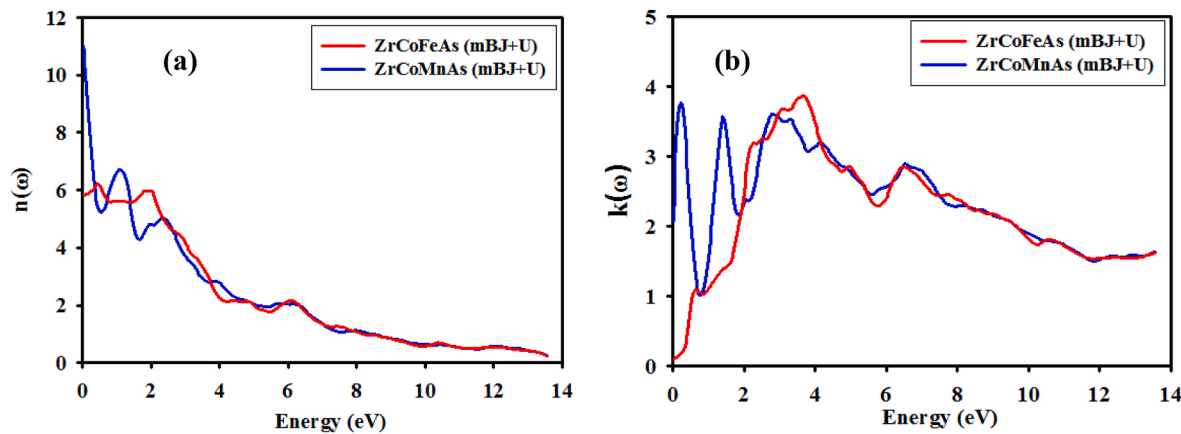
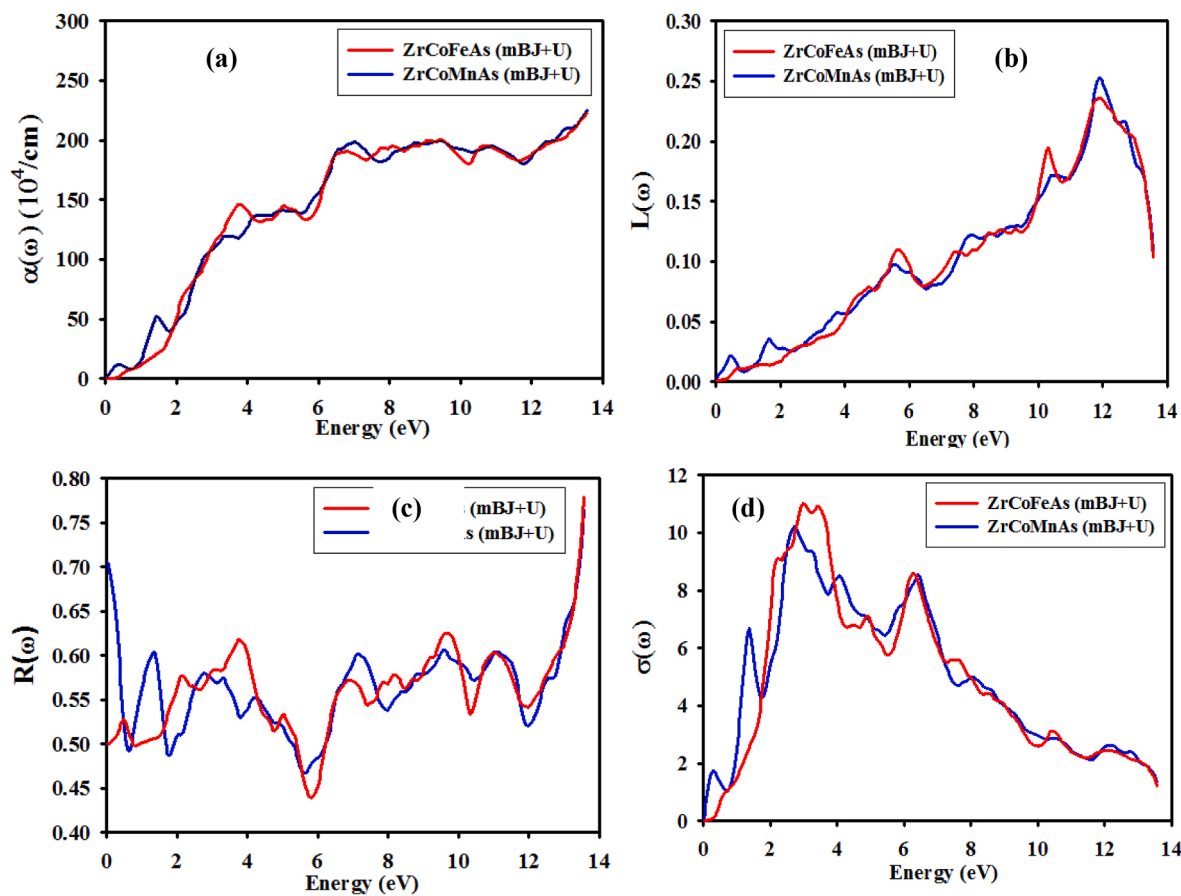


Fig. 11. (a) Refractive index and (b) extinction coefficient.

Fig. 12. Computed (a) absorption coefficient $\alpha(\omega)$, (b) energy loss function $L(\omega)$, (c) reflectivity $R(\omega)$, and (d) optical conductivity of ZrCoFeAs and ZrCoMnAs.

with the other speculated thermoelectric (TE) properties. It is expressed as $ZT = S^2\sigma T/\kappa$ and has direct proportionality with the Seebeck coefficient (S), direct linearity with the electrical conductivity (σ), absolute temperature (T), and an inverse relationship with the thermal conductivity (κ). It is noticed that the figure of merit (Fig. 14 (b)) of all alloys initially rapidly increase with temperature and reaches a maximum at temperatures near 1400K. The both alloys are exhibiting the best performance with the maximum ZT value of 1.1 at 1400K, which is very promising for thermoelectric applications. The experimental stability could impact the application of these compounds crystals as thermoelectric materials. To the best of our knowledge, none of these compounds have been experimentally synthesized to date. We hope our

research will serve as a reference for future studies (see Fig. 15).

Fig. 15 (a) provides a comprehensive overview of the Hall effect response at various temperatures. The sign of RH indicates the characteristics of the dominant charge carriers, being positive when the majority of carriers are holes and negative when they are electrons. The Hall coefficient value for these materials across the entire temperature range is positive, indicating that holes are the primary contributors to the generation of Hall voltage in the presence of a magnetic field.

Fig. 15 (b) displays the relationship between the electronic heat capacity (c) and temperature for both alloys. The (c) remains unaffected by the size of the system and provides a measure of how much the substance's temperature changes per unit of absorbed heat [65,66]. At

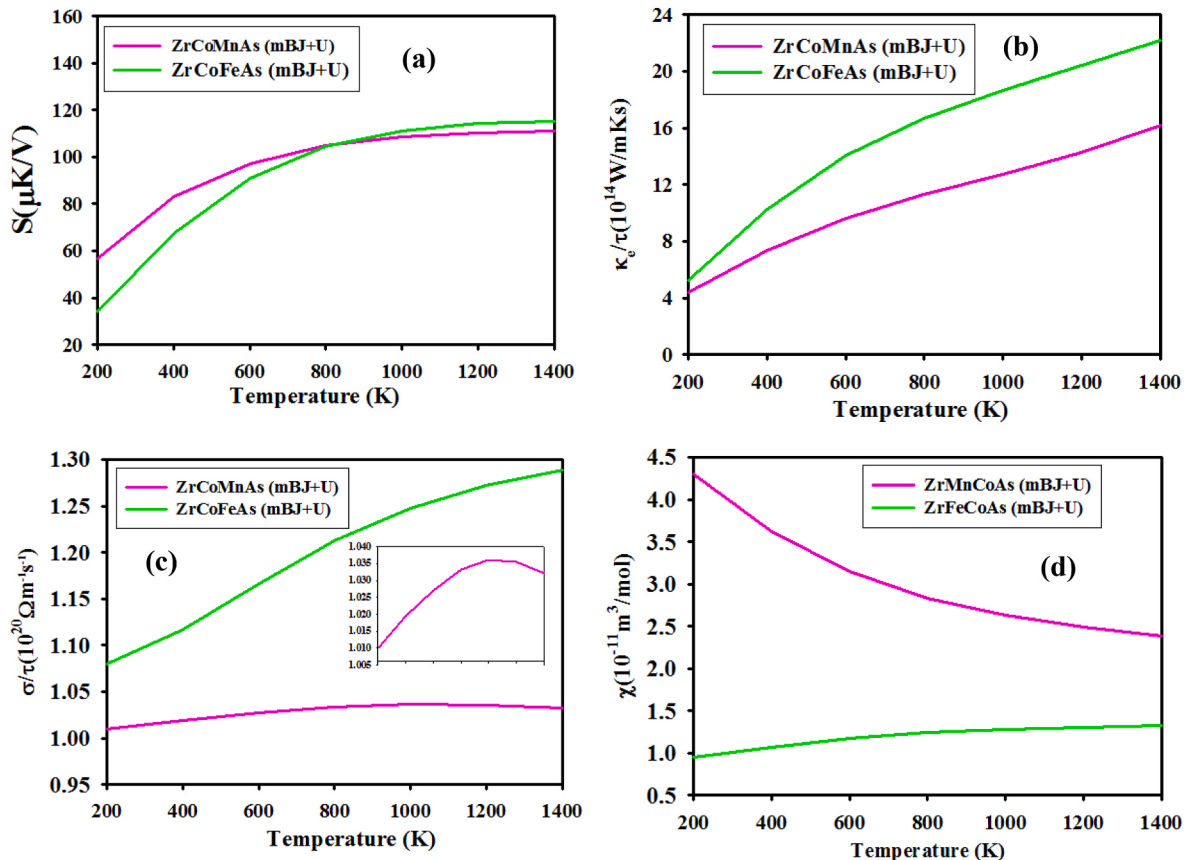


Fig. 13. The evaluated (a) Seebeck coefficient $S(T)$, (b) electronic thermal conductivity $\kappa_e(T)$, (c) electrical conductivity $\sigma(T)$, and (d) Magnetic susceptibility $\chi(T)$ for ZrCoFeAs and ZrCoMnAs, respectively.

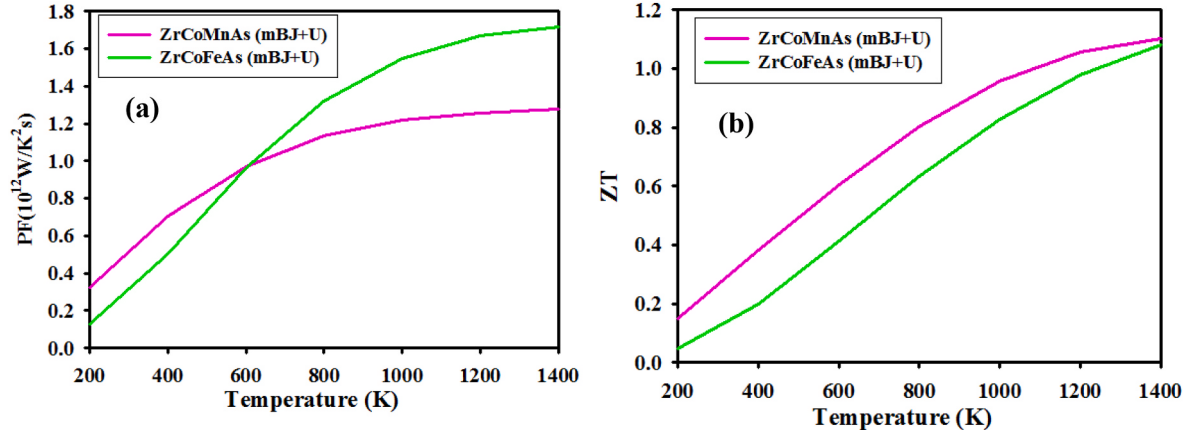


Fig. 14. (a) Power factor and (b) figure of merit plots versus temperature of ZrCoFeAs and ZrCoMnAs, respectively.

room temperature, we notice that this property exhibits $4.8 \text{ J mol}^{-1} \text{ K}^{-1}$ and $2.6 \text{ J mol}^{-1} \text{ K}^{-1}$ for ZrCoFeAs and ZrCoMnAs, respectively. However, as the temperature increases, the electronic heat capacity (c) begins to rise, with a more significant increase observed in both alloys.

4. Conclusion

This work investigated two novel quaternary Heusler alloys type ZrCoYAs ($Y = \text{Fe}$ and Mn) using a theoretical prediction based on DFT calculations.

According to structural properties, the most stable atomic arrangement is ferromagnetic Y-type-III. The calculation of formation energy

provided additional evidence for this, and her negative value indicated that our alloys are promising to be synthesized. According to the elastic properties, the examined alloys are mechanically stable in their energetically stable phase.

The electronic properties calculations predict a metallic character with GGA-PBE and GGA + U. However, the mBJ-GGA-PBE and mBJ-GGA + U predict a half-metallic character behavior with a band gap in the spin-down channel for our alloys. The mBJ-GGA-PBE and mBJ-GGA + U approximations were also applied to improve the electronic and magnetic properties. The gap and half-metal character are caused by the hybridization of the d states of the Zr, Co, Fe and Mn atoms. The magnetic moment values are integer and obey the Slater-Pauling rule, 1.00

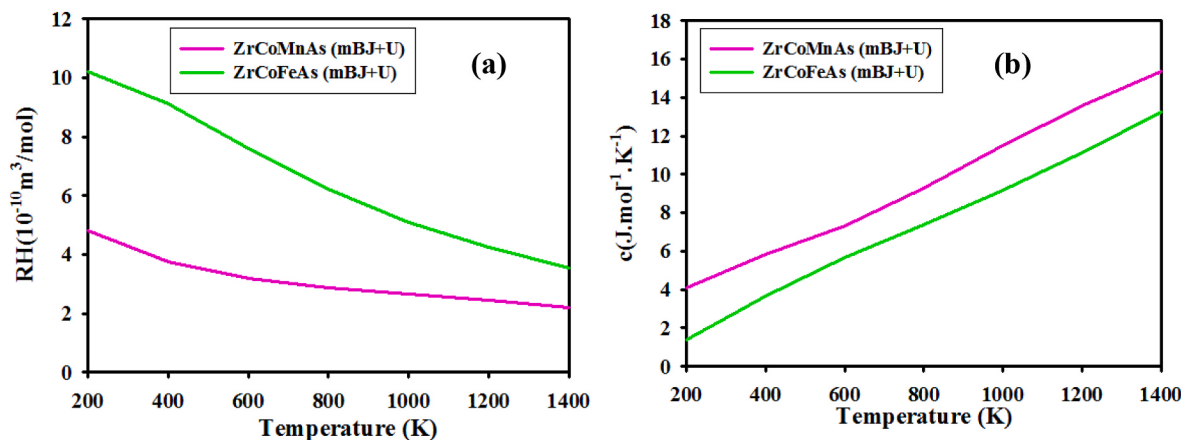


Fig. 15. Calculated plots of (a) Hall coefficient and (b) specific heat capacity for ZrCoFeAs and ZrCoMnAs in the temperature range 200–1400 K.

μB and $2.00 \mu\text{B}$ for ZrCoMnAs and ZrCoFeAs, respectively. Based on the new model and MFA, ZrCoMnAs and ZrCoFeAs have predicted Curie temperatures of 204 K (421 K using MFA) and 385 K (1627 K using MFA), respectively. Thus, we find that our alloys are suited for application in spintronics devices.

The optical and thermoelectric properties of the ZrCoFeAs and ZrCoMnAs are theoretically investigated. The mBJ-GGA + U method is selected to investigate all these properties. The obtained result of the absorption coefficient increases rapidly in the visible region and the maximum values are in ultraviolet light. These properties make these alloys promising candidates for optoelectronic applications. The Boltz-TraP code is utilized to assess the thermoelectric properties within a temperature range of 200K–1400K. The positive Seebeck coefficient ensures p-type Heusler. Additionally, it is observed that the conductivities of both substances rise as the temperature increases. The predicted figure of merit (ZT) implies that they are very promising for thermoelectric applications. Given the comparatively high conductivities, they could potentially be utilized in the aerospace industry for manufacturing high-temperature conductive components. Therefore, the significant increase in PF suggests a strong potential for both alloys in commercial thermoelectric applications.

The experimental study for confirmations is crucial because our study can be regarded as the first quantitative theoretical predictions of the structural, magneto-electronic, elastic, mechanical, and thermoelectric properties for these alloys.

CRediT authorship contribution statement

O. Baraka: Writing – review & editing, Visualization, Methodology, Investigation, Conceptualization. **S. Malki:** Writing – review & editing, Validation, Methodology, Conceptualization. **L. El farh:** Writing – review & editing, Validation. **A. Yakoubi:** Writing – review & editing, Validation. **D. Sébilleau:** Writing – review & editing, Validation.

Declaration of competing interest

The authors declare that they have no known competing financial interests or personal relationships that could have appeared to influence the work reported in this paper.

Data availability

No data was used for the research described in the article.

References

- [1] Y. Jin, Novel half-metallic and spin-gapless heusler compounds. Theses, Dissertations, and Student Research: Department of Physics and Astronomy, 2017, p. 37.
- [2] C. Felser, L. Wollmann, S. Chadov, G.H. Fecher, S.S.P. Parkin, in: C. Felser, A. Hirohata (Eds.), Heusler Compounds: Properties, Growth, Applications, Springer International Publishing, Cham, 2016, pp. 37–48, <https://doi.org/10.1007/978-3-319-21449-8>.
- [3] T.C. Chibueze, C.E. Ekuma, A.T. Raji, F.I. Ezema, C.M.I. Okoye, Tetragonal and uniaxial strains in pristine and doped half-Heusler AuMnSn alloy, *J. Alloys Compd.* 848 (2020) 156186, <https://doi.org/10.1016/j.jallcom.2020.156186>.
- [4] T.C. Chibueze, A.T. Raji, C.E. Ekuma, Conservation of the robust ferromagnetic half-conductivity in 110-surface half-Heusler NaCrAs alloy by strains and defects, *Surface. Interfac.* 40 (2023) 103091, <https://doi.org/10.1016/j.surfin.2023.103091>.
- [5] D. Kieven, R. Klenk, S. Naghavi, C. Felser, T. Gruhn, I-II-V half-Heusler compounds for optoelectronics: ab initio calculations, *Phys. Rev. B* 81 (2010) 075208, <https://doi.org/10.1103/PhysRevB.81.075208>.
- [6] S. Ouardi, G.H. Fecher, B. Balke, X. Kozina, G. Stryganyuk, C. Felser, S. Lowitzer, D. Kodderitzsch, H. Ebert, E. Ikenaga, Electronic transport properties of electron- and hole-doped semiconducting C1_b Heusler compounds: NiTi_{1-x}M_xSn (M=Sc,V), *Phys. Rev. B* 82 (2010) 085108, <https://doi.org/10.1103/PhysRevB.82.085108>.
- [7] Fr Heusler, Verh. d. DPG 5 (1903) 219, <https://doi.org/10.1051/jphystap:019040030021201>.
- [8] X. Wang, Z. Cheng, J. Wang, X. Wang, G. Liu, Recent advances in the Heusler based spin-gapless semiconductors, *J. Mater. Chem. C* 4 (2016) 7176, <https://doi.org/10.1039/C6TC01343K>.
- [9] X. Wang, Z. Cheng, J. Wang, G. Liu, A full spectrum of spintronic properties demonstrated by a C1b-type Heusler compound Mn₂Sn subjected to strain engineering, *J. Mater. Chem. C* 4 (2016) 8535, <https://doi.org/10.1039/C6TC02526A>.
- [10] L.Y. Wang, X.T. Wang, R.K. Guo, T.T. Lin, G.D. Liu, Electronic and magnetic properties of Cr-Mn-Ni-Al compound with LiMgPdSb-type structure, *Solid State Commun.* 244 (2016) 38–42, <https://doi.org/10.1016/j.ssc.2016.06.019>.
- [11] H.S. Goripati, T. Furubayashi, Y.K. Takahashi, K. Hono, Current-perpendicular-to-plane giant magnetoresistance using Co₂Fe(Ga_{1-x}Ge_x) Heusler alloy, *J. Appl. Phys.* 113 (2013) 04390, <https://doi.org/10.1063/1.4788672>.
- [12] L. Bainsla, K.G. Suresh, Equiatomic quaternary Heusler alloys: a material perspective for spintronic applications, *Appl. Phys. Rev.* 3 (2016) 03110, <https://doi.org/10.1063/1.4959093>.
- [13] P. Klaer, B. Balke, V. Alijani, J. Winterlik, G.H. Fecher, C. Felser, H.J. Elmers, Element-specific magnetic moments and spin resolved density of states in CoFeMnZ ($Z = \text{Al, Ga, Si, Ge}$), *Phys. Rev. B* 84 (14) (2011) 144413, <https://doi.org/10.1103/PhysRevB.84.144413>.
- [14] M.H. Elahmar, H. Rached, D. Rached, R. Khenata, G. Murtaza, S. BinOmran, W. K. Ahmed, Structural, mechanical, electronic and magnetic properties of a new series of quaternary Heusler alloys CoFeMnZ ($Z = \text{Si, As, Sb}$): a first-principle study, *J. Magn. Magn. Mater.* 393 (2015) 165–174, <https://doi.org/10.1016/j.jmmm.2015.05.019>.
- [15] L. Xiong, L. Yi, G. Gao, Search for half-metallic magnets with large half-metallic gaps in the quaternary Heusler alloys CoFeTiZ and CoFeVZ ($Z = \text{Al, Ga, Si, Ge, As, Sb}$), *J. Magn. Magn. Mater.* 360 (2014) 98–103, <https://doi.org/10.1016/j.jmmm.2014.02.050>.
- [16] Y. Zhang, Z. Liu, G.T. Li, X.Q. Ma, G.D. Liu, Magnetism, band gap and stability of half-metallic property for the quaternary Heusler alloys CoFeTiZ ($Z = \text{Si, Ge, Sn}$), *J. Alloys Compd.* 616 (2014) 449–453, <https://doi.org/10.1016/j.jallcom.2014.07.165>.
- [17] Y. Gao, X. Gao, The half-metallicity of LiMgPdSn-type quaternary Heusler alloys FeMnScZ ($Z = \text{Al, Ga, In}$): a first-principle study, *AIP Adv.* 5 (5) (2015) 057157, <https://doi.org/10.1063/1.4921900>.

- [18] M. Benkabou, H. Rached, A. Abdellaoui, D. Rached, R. Khenata, M.H. Elahmar, B. Abidri, N. Benkhettou, S. Bin-Omran, Electronic structure and magnetic properties of quaternary Heusler alloys CoRhMnZ ($Z = Al, Ga, Ge$ and Si) via first-principle calculations, *J. Alloys Compd.* 647 (2015) 276–286, <https://doi.org/10.1016/j.jallcom.2015.05.273>.
- [19] M. Khodami, F. Ahmadian, First-principles study of magnetism and half-metallic properties for the quaternary Heusler alloys CoMnTiZ ($Z = P, As$, and Sb), *J. Supercond. Nov. Magnetism* 28 (10) (2015) 3027–3035, <https://doi.org/10.1007/s10948-015-3126-2>.
- [20] S. Berri, First-principles study on half-metallic properties of the CoMnCrSb quaternary Heusler compound, *J. Supercond. Nov. Magnetism* 29 (5) (2016) 1309–1315, <https://doi.org/10.1007/s10948-016-3404-7>.
- [21] K. Benkaddour, A. Chahed, A. Amar, H. Rozale, A. Lakdja, O. Benhalal, A. Sayede, First-principles study of structural, elastic, thermodynamic, electronic and magnetic properties for the quaternary Heusler alloys CoRuFeZ ($Z = Si, Ge, Sn$), *J. Alloys Compd.* 687 (2016) 211–220, <https://doi.org/10.1016/j.jallcom.2016.06.104>.
- [22] S. Bahramian, F. Ahmadian, Half-metallicity and magnetism of quaternary Heusler compounds CoRuTiZ ($Z = Si, Ge$, and Sn), *J. Magn. Magn Mater.* 424 (2017) 122–129, <https://doi.org/10.1016/j.jmmm.2016.10.020>.
- [23] D. Rani, K.G. Suresh, A.K. Yadav, S.N. Jha, D. Bhattacharyya, M.R. Varma, A. Alam, Structural, electronic, magnetic, and transport properties of the equiatomic quaternary Heusler alloy CoRhMnGe: theory and experiment, *Phys. Rev. B* 96 (18) (2017) 184404, <https://doi.org/10.1103/PhysRevB.96.184404>.
- [24] A. Bahnes, A. Boukortt, H. Abbassa, D.E. Aimouch, R. Hayn, A. Zaoui, Half-metallic ferromagnets behavior of a new quaternary Heusler alloys CoFeCrZ ($Z = P$, and Sb): ab-initio study, *J. Alloys Compd.* 731 (2018) 1208–1213, <https://doi.org/10.1016/j.jallcom.2017.10.178>.
- [25] A.R. Chandra, V. Jain, N. Lakshmi, V.K. Jain, K. Soni, R. Jain, Electronic structure properties of new equiatomic CoCuMnZ ($Z = In, Sn, Sb$) quaternary Heusler alloys: an ab-initio study, *J. Alloys Compd.* 748 (2018) 298–304, <https://doi.org/10.1016/j.jallcom.2018.03.143>.
- [26] G. Forozani, A.A.M. Abadi, S.M. Baizeeaa, A. Gharaati, Structural, electronic and magnetic properties of ZrCoIrSi quaternary Heusler alloy: first-principles study, *J. Alloys Compd.* (2019), <https://doi.org/10.1016/j.jallcom.2019.152449>.
- [27] S. Idrissi, H. Labrim, S. Zitzi, L. Bahmad, Investigation of the physical properties of the equiatomic quaternary Heusler alloy CoYCrZ ($Z = Si$ and Ge): a DFT study, *Appl. Phys. A* (2020) 126–190, <https://doi.org/10.1007/s00339-020-3354-6>.
- [28] V. Aravindan, A.K. Rajarajan, V. Vijayanarayanan, M. Mahendran, Investigation of the physical properties of CoRuVAL equiatomic quaternary Heusler alloy using first-principles calculations, *Phys. B Condens. Matter* 647 (2022) 414370, <https://doi.org/10.1016/j.physb.2022.414370>.
- [29] V. Aravindan, A.K. Rajarajan, V. Vijayanarayanan, M. Mahendran, First-principles investigations of the half-metallic ferromagnetic LaCoTiIn equiatomic quaternary Heusler alloy for spintronics, *Functional Materials Letters* 15 (2022) 2251011, <https://doi.org/10.1142/S1923604722510110>.
- [30] V. Aravindan, A.K. Rajarajan, V. Vijayanarayanan, M. Mahendran, First-principles calculations on novel Co-based equiatomic quaternary heusler alloys for spintronics, *Mater. Sci. Semicond. Process.* 150 (2022) 106909, <https://doi.org/10.1016/j.mssp.2022.106909>.
- [31] J.C. Slater, Energy band calculations by the augmented plane wave method, *Adv. Quant. Chem.* 1 (1964) 5564, [https://doi.org/10.1016/S0065-3276\(08\)60374-3](https://doi.org/10.1016/S0065-3276(08)60374-3).
- [32] P. Blaha, K. Schwarz, F. Tran, R. Laskowski, G.K.H. Madsen, L.D. Marks, WIEN2k: an APW+lo program for calculating the properties of solids, *J. Chem. Phys.* 152 (2020) 074101, <https://doi.org/10.1063/1.5143061>.
- [33] P. Hohenberg, W. Kohn, Inhomogeneous electron gas, *Phys. Rev.* 136 (1964) 864, <https://doi.org/10.1103/PhysRev.136.B864>.
- [34] W. Kohn, L.J. Sham, Self-consistent equations including exchange and correlation effects, *Phys. Rev.* 140 (1965) 1133, <https://doi.org/10.1103/PhysRev.140.A1133>.
- [35] J.P. Perdew, S. Burke, M. Ernzerhof, Generalized gradient approximation made simple, *Phys. Rev. Lett.* 77 (1996) 3865, <https://doi.org/10.1103/PhysRevLett.77.3865>.
- [36] J.P. Perdew, S. Burke, Y. Wang, Generalized gradient approximation for the exchange-correlation hole of a many-electron system, *Phys. Rev. B* 54 (1996) 16533, <https://doi.org/10.1103/PhysRevB.54.16533>.
- [37] V.I. Anisimov, J. Zaanen, O.K. Andersen, *Phys. Rev. B* 44 (1991) 943, <https://doi.org/10.1103/PhysRevB.44.943>.
- [38] A.D. Becke, E.R. Johnson, A simple effective potential for exchange, *J. Chem.* (2006) 124, <https://doi.org/10.1063/1.2213970>.
- [39] F. Tran, P. Blaha, Accurate band gaps of semiconductors and insulators with a semilocal exchange-correlation potential, *Phys. Rev. Lett.* 102 (2009) 226401, <https://doi.org/10.1103/PhysRevLett.102.226401>.
- [40] F.D. Murnaghan, The compressibility of media under extreme pressures, *Proc. Natl. Acad. Sci. U.S.A.* 30 (1944) 244, <https://doi.org/10.1073/pnas.30.9.244>.
- [41] M. Jamal, S.J. Asadabadi, I. Ahmad, H.R. Aliabad, Elastic constants of cubic crystals, *Comput. Mater. Sci.* 95 (2014) 592–599, <https://doi.org/10.1016/j.commatsci.2014.08.027>.
- [42] J. Wang, S. Yip, S.R. Phillpot, D. Wolf, Crystal instabilities at finite strain, *Phys. Rev. Lett.* 71 (1993) 4182–4185, <https://doi.org/10.1103/PhysRevLett.71.4182>.
- [43] A. Yakoubi, O. Baraka, B. Bouhafs, Structural and electronic properties of the Laves phase based on rare earth type BaM_2 ($M = Rh, Pd, Pt$), *Results Phys.* 2 (2012) 58–65, <https://doi.org/10.1016/j.rinp.2012.06.001>.
- [44] A. Bouhemadou, R. Khenata, M. Kharoubi, T. Seddk, A.H. Reshak, Y. Al-Douri, FP-APW+lo calculations of the elastic properties in zinc-blende III-P compounds under pressure effects, *Comput. Mater. Sci.* 45 (2009) 474–479, <https://doi.org/10.1016/j.commatsci.2008.11.013>.
- [45] M.E. Fine, L.D. Brown, H.L. Marcus, Elastic constants versus melting temperature in metals, *Scripta Metall.* 18 (1984) 951–956, [https://doi.org/10.1016/0036-9748\(84\)90267-9](https://doi.org/10.1016/0036-9748(84)90267-9).
- [46] Laihinkima, C.E. Ekuma, T.C. Chibueze, L.A. Fomin, I.V. Malikov, L. Zadeng, D. P. Rai, Electronic, magnetic, vibrational, and X-ray spectroscopy of inverse full-Heusler Fe 2 IrSi alloy, *Phys. Chem. Chem. Phys.* 23 (2021) 11876–11885, <https://doi.org/10.1039/DICP00418B>.
- [47] K. Ozdogan, E. Sasioglu, I. Galanakis, Slater-Pauling behavior in LiMgPdSn-type multifunctional quaternary Heusler materials: half-metallicity, spin-gapless and magnetic semiconductors, *J. Appl. Phys.* 113 (2013) 193903, <https://doi.org/10.1063/1.4805063>.
- [48] X.Q. Chen, R. Podloucky, P. Rogl, Ab initio prediction of half-metallic properties for the ferromagnetic Heusler alloys Co_2MSi ($M = Ti, V, Cr$), *J. Appl. Phys.* 100 (2006) 113901, <https://doi.org/10.1063/1.2374672>.
- [49] G. Arfken, *Mathematical Methods for Physicists*, third ed., Academic, ca, 1985 (san diego).
- [50] K.R. Waters, J. Mobley, J.G. Miller, Causality-imposed (Kramers-Kronig) relationships between attenuation and dispersion, *IEEE Trans. Ultrason. Ferroelectrics Freq. Control* 52 5 (2005) 822–823, <https://doi.org/10.1109/TUFFC.2005.1503968>.
- [51] A. Dey, A first-principles study of TiX_2 ($X = Se, Te$, and Te) compounds optical properties under the effect of externally applied electric field and strain, *Phys. Solid State* 62 (2020) 1905–1915, <https://doi.org/10.1134/S1063783420100042>.
- [52] S.A. Dar, R. Sharma, V. Srivastava, U.K. Sakalle, Investigation on the electronic structure, optical, elastic, mechanical, thermodynamic and thermoelectric properties of wide band gap semiconductor double perovskite Ba_2InTaO_6 , *RSC Adv.* 9 17 (2019) 9522–9532, <https://doi.org/10.1039/C9RA00313D>.
- [53] H.S. Ashour, Near-zero-refractive-index structure at optical frequencies, *Adv. Condens. Matter Phys.* 328402 (2013), <https://doi.org/10.1155/2013/328402>.
- [54] M. Ahmad, G. Rehman, L. Ali, M. Shafiq, R. Iqbal, R. Ahmad, I.M. Ahmad, Structural, electronic and optical properties of $CsPbX_3$ ($X = Cl, Br, I$) for energy storage and hybrid solar cell applications, *J. Alloys Compd.* 705 (2017) 828–839, <https://doi.org/10.1016/j.jallcom.2017.02.147>.
- [55] S. Saidi, S. Zriouel, L.B. Drissi, M. Maaroufi, A DFT study of electro-optical properties of kesterite Ag_2CdSnX_4 for photovoltaic applications, *Phys. E Low-dimens. Syst. Nanostruct.* 103 (2018) 171–179, <https://doi.org/10.1016/j.physe.2018.05.036>.
- [56] F. Parvin, M.A. Hossain, I. Ahmed, K. Akter, A.K.M.A. Islam, First-principles calculations to investigate mechanical, optoelectronic and thermoelectric properties of half-Heusler p-type semiconductor $BaAgP$, *Results Phys.* 23 (2021) 104068, <https://doi.org/10.1016/j.rinp.2021.104068>.
- [57] A. Abada, N. Marbouh, Study of new d^0 half-metallic half-Heusler alloy $MgCaB$: first-principles calculations, *J. Supercond. Nov. Magnetism* 33 (2020) 889–899, <https://doi.org/10.1007/s10948-019-05288-1>.
- [58] Y.F. Li, Y.C. Ding, B. Xiao, Y.H. Cheng, Anisotropic electrical and lattice transport properties of ordered quaternary phases Cr_2TiAlC_2 and Mo_2TiAlC_2 : a first principles study, *Phys. Lett.* 380 44 (2016) 3748–3755, <https://doi.org/10.1016/j.physleta.2016.09.015>.
- [59] N. Yaqoob, G. Muratza, M.W. Iqbal, N.A. Noor, A. Mahmood, S.M. Ramay, N.Y. Al-Garadi, Study of half metallic nature and transport properties of $XMnSe_2$ ($X = Ca, Sr$ and Ba) compounds via ab-initio calculations, *J. Mater. Res. Technol.* 9 (2020) 10511–10519, <https://doi.org/10.1016/j.jmr.2020.07.037>.
- [60] C. Kittel, *Introduction to Solid State Physics*, John Wiley & Sons, inc, 2005.
- [61] A. Wahab, B. Sabir, N.A. Kattan, N. Yaqoob, E. Algrafi, G. Muratza, I.A. Jamil, Ab initio study of electronic, optical and thermoelectric character of intermetallic compounds XGa_3 ($X = Fe, Ru, Os$), *Opt. Quant. Electron.* 52 (2020) 1–15, <https://doi.org/10.1007/s11082-020-02332-6>.
- [62] E. Haque, M.A. Hossain, Elastic, magnetic, transport and electronic properties of noncentrosymmetric M_2Mo_3N ($M = Fe, Co, Ni, Rh$): A first-principles study, *J. Alloys Compd.* 748 (2018) 117–126, <https://doi.org/10.1016/j.jallcom.2018.03.151>.
- [63] M. Boudjelal, M. Batouche, T. Seddk, T. Antri, N. Badi, S. Bentata, S. Bin Omran, Structural, magnetic, and optoelectronic properties of new ferromagnetic semiconductors $Cd_{0.75}Os_{0.25}S$ and $Cd_{0.75}Ir_{0.25}S$: insight from DFT computations, *Opt. Quant. Electron.* 54 (2022) 716, <https://doi.org/10.1007/s11082-022-04073-0>.
- [64] T. Ramachandran, R. Ne, P. Pp, Enhanced Thermoelectric Properties of $BiCoO_3$ by Nickel Substitution, *Materials Sciences and Applications*, 2013, <https://doi.org/10.4236/msa.2013.412104>.
- [65] S.A. Khandy, D.C. Gupta, Structural, elastic and thermo-electronic properties of paramagnetic perovskite $PbTaO_3$, *RSC Adv.* 6 (53) (2016) 48009–48015, <https://doi.org/10.1039/C6RA10468A>.
- [66] M.E. Ketfi, H. Bennacer, S.S. Essaoud, M.I. Ziane, A. Boukortt, Computational evaluation of optoelectronic, thermodynamic and electron transport properties of $CuYZ_2$ ($Z = S, Se$ and Te) chalcogenides semiconductors, *Mater. Chem. Phys.* 277 (2022) 125553, <https://doi.org/10.1016/j.matchemphys.2021.125553>.